



# Two-Step SPD Processing of a Trimodal Al-Based Nano-Composite

Yuzheng Zhang\*, Shima Sabbaghianrad, Hanry Yang, Troy D. Topping, Terence G. Langdon, Enrique J. Lavernia, Julie M. Schoenung, Steven R. Nutt

\* E-mail: yuzhengz@usc.edu

**Abstract:** An ultrafine-grained (UFG) aluminum nano-composite was fabricated using two severe plastic deformation steps: cryomilling of powders (and subsequent consolidation of blended powders by forging) followed by high-pressure torsion (HPT). The forged bulk composite featured a trimodal structure comprised of UFG, coarse grain (CG) regions, and ceramic particles. The additional HPT processing introduced finer grain sizes and altered the morphology and spatial distribution of the ductile CG regions. As a result, both strength and ductility increased substantially compared to those of the Al nano-composite prior to HPT. The increases were attributed to the more optimal shape and spacing of the CG regions which promoted uniform elongation and yielding during tensile loading. Microstructural changes were characterized at each processing step to establish the evolution of microstructure and to elucidate structure-property relationships. The toughening effect of the CG regions was documented *via* fracture analysis, providing a potential strategy for designing microstructures with enhanced strength and toughness.

## 1. INTRODUCTION

Ultrafine-grained (UFG) materials, characterized by average grain sizes of  $<1\ \mu\text{m}$ , have been studied extensively because of their unique properties.[1–7] Because of the small grain size and large volume fraction of the grain boundary regions, UFG materials exhibit greater strength Y Zhang, S Sabbaghianrad, H Yang, T Topping, T Langdon, E Lavernia, J Schoenung, and S Nutt, “Two-step SPD processing of a trimodal Al-based nano-composite” Metall Trans Sept (2015) DOI: 10.1007/s11661-015-3151-6



than their coarse grain (CG) counterparts. The Hall–Petch effect predicts an increase in yield strength with a decrease in grain size.[8,9] However, UFG materials are inherently brittle at room temperature due to the suppression of plasticity mechanisms. Additions of ceramic particles impart additional strength but further reduce ductility and toughness. In this work, we present an approach for increasing the toughness of a UFG Al-based metal matrix nano-composite using two-step severe plastic deformation (SPD) processing.

SPD processing describes a set of top-down fabrication techniques used in making UFG materials.[10,11] In SPD methods, a high level of plastic strain is applied to coarse grain (CG) materials to refine the grain structure to the UFG regime.[12] Unlike bottom-up techniques, such as electrodeposition or vapor deposition, SPD techniques can be used to produce UFG materials with full density in bulk forms other than thin films. In this work, the aluminum alloy (AA) 5083 was selected as the base material due to the low density, weldability, corrosion resistance, and widespread use in automobile, aerospace, marine, and defense applications.[13–15] However, the relatively low strength of AA 5083 (relative to steel and titanium alloys) limits applications in high load-bearing structures and ballistic protection. Therefore, increasing the strength of AA 5083 using SPD techniques represents a practical approach to expand the utility of this alloy to a broader range of engineering applications. In this study, we describe the synthesis of a bulk UFG AA 5083 nano-composites using a combination of cryomilling and high-pressure torsion (HPT).

Cryomilling,[16] a variant of ball milling, was performed to refine the grain structure beyond the refinement typically possible by other SPD techniques. During cryomilling, the powders were repeatedly fractured and cold-welded while immersed in a slurry of stainless steel balls and liquid nitrogen. During this process, the grain size of AA 5083 powders was refined to



the nanocrystalline regime via severe plastic deformation.[16] The liquid nitrogen dissipated heat generated during milling, thereby suppressing recrystallization and grain growth while simultaneously inhibiting oxidation at fractured surfaces and promoting the formation of nitride phases.[17–19] Hot vacuum degassing was performed to remove residual gas contamination, and a two-step consolidation process was carried out to consolidate the powders into bulk forms. Previous studies have shown that the as-milled powders exhibited an average grain size of less than 100 nm.[16] The subsequent degassing and consolidation processes introduced moderate grain growth, leading to a final average grain size of ~500 nm in the bulk form.[16]

Cryomilled AA 5083 is inherently brittle due to the lack of effective plasticity mechanisms. In early efforts to improve toughness, unmilled CG powders were blended with milled powders before consolidating the powders to bulk form.[20,21] The microstructure after consolidation consisted of CG regions evenly dispersed in a UFG matrix, and thus a bimodal grain size distribution could be fabricated. The introduction of CG regions in a UFG matrix reportedly imparts unusual deformation and fracture mechanisms not unlike ductile-phase toughening. For example, it was observed that the bimodal structure of an Al-Mg alloy exhibited increased ductility with a moderate sacrifice in strength.[21,22] Similarly, it was reported that the CG regions in the bimodal microstructure not only improved the global ductility, but also delayed plastic instability.[20] Another study of bimodal aluminum showed that the plastic strain was localized in the CG regions during deformation.[23]

To afford ballistic protection to military vehicles, researchers have reinforced UFG aluminum alloys with boron carbide (B<sub>4</sub>C) particles, adding the particles during cryomilling[24,25] to produce a trimodal structure (UFG matrix, CG region, and B<sub>4</sub>C particles) as



described later in this work. The trimodal AA 5083 exhibited a two-fold increase in tensile strength compared to a conventional alloy (see Section III–D). This remarkable increase in strength was attributed to a combination of B<sub>4</sub>C strengthening via load transfer, grain boundary strengthening, and Orowan strengthening from dispersoids.[26] During deformation, micro-voids nucleated in the brittle UFG matrix and evolved into cracks. When a propagating crack reached a ductile CG region, the crack tip was blunted and arrested due to the enhanced plasticity of the CG regions. However, in a previous study, we observed that this toughening mechanism was ineffective because the spacing and the morphology of the CG regions were far from optimal.[27] For effective ductile-phase toughening, the size and spacing of the ductile regions should be comparable to the plastic zone size of the brittle matrix.[28] Based on a previous estimate,[27] the optimal size and spacing of the CG regions for effective toughening are ~10 to 50  $\mu\text{m}$ . In this work, we explore an approach to achieve near-optimal spacing and shapes of the CG regions by applying post-consolidation shear strain using HPT.

HPT is another SPD technique for making ultrafine-grained materials in disk or ring form.[29] During HPT, a large amount of torsional strain is applied on a disk sample under high compressive pressure (typically ~6.0 GPa).[29] In HPT, a disk sample is typically placed in the depressions between two anvils and the lower anvil rotates to produce torsional straining with a radial gradient (largest strain on periphery and lowest in center). The compressive constraint ensures that the sample can sustain large amounts of strain without fracture.[29] Processing by HPT was conducted on the trimodal AA 5083 as a secondary SPD process to reduce the spacing of the CG regions and impart more lamellar shapes. In the following sections, we describe a trimodal



microstructure reshaped by HPT and investigate the effects of this structure on the mechanical behavior and failure mechanism of trimodal AA 5083.

## 2. EXPERIMENTAL PROCEDURE

### 2.1. Material Synthesis

Gas-atomized AA 5083 powder (Al-4.4Mg-0.7Mn-0.15Cr wt pct) together with submicron B<sub>4</sub>C particles was ball milled (32:1 ball-to-powder ratio) in a liquid nitrogen slurry for 12 hours using a modified 1S Szegvari attritor at 180 rpm. Afterward, unmilled (as atomized) AA 5083 powder was blended with the milled powder to reach a trimodal composition of 66.5 vol pct UFG Al, 30 vol pct CG Al, and 3.5 vol pct B<sub>4</sub>C reinforcing particles. The mixed powder was sealed in a container for hot vacuum degassing at 773 K (500 °C) for 20 hours. The degassed powders were then consolidated using dual-mode dynamic (DMD) forging, formerly known as quasi-isostatic or Ceracon™ forging.

After DMD forging, trimodal samples were machined into 9.8-mm disks as shown in Figure 1. The plane normal of the disk was parallel to the forging direction. The trimodal disks were abrasive-polished to a final thickness of ~0.82 mm. These disks were processed by HPT at room temperature under a compressive pressure of 6.0 GPa. The HPT processing in this work was conducted in a quasi-constrained condition at a rotating speed of 1 rpm through total numbers of 1/4, 1, and 5 turns (revolutions). The processed disk had a final thickness of ~0.69 mm with minor material outflow at the periphery. Subsequent to HPT, samples were annealed for one hour at 373 K, 473 K, 573 K, and 673 K (100 °C, 200 °C, 300 °C, and 400°C), individually.

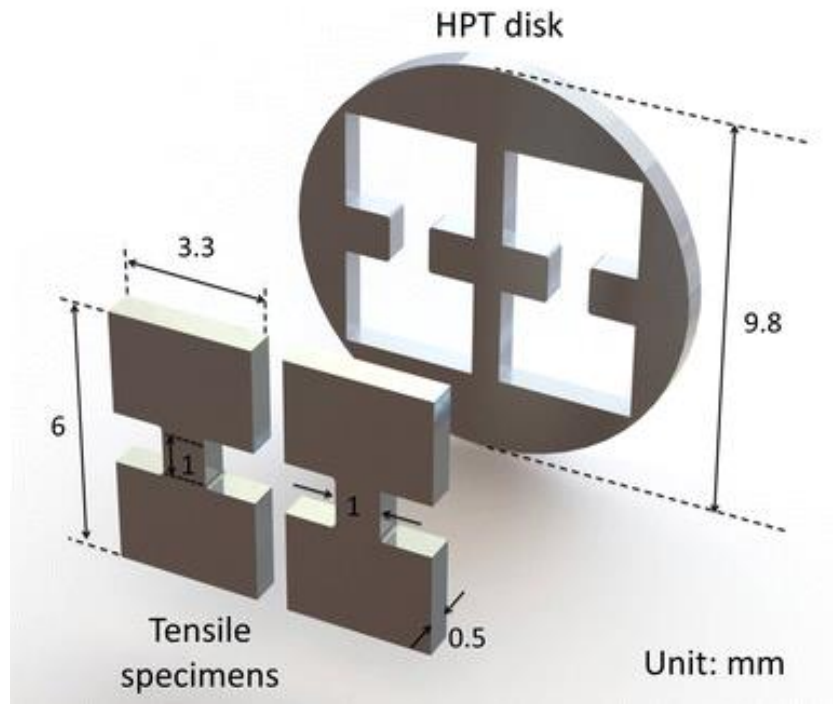


*Fig. 1 Dimensions of the HPT disk and two miniature dog-bone specimens machined from the disk*

## 2.2. Microstructure

The microstructure of the sample processed by HPT was observed using a digital light microscope (VHX-600, Keyence, USA) after preparing polished sections using SiC papers and a colloidal silica suspension. The grain size distribution in the CG regions was measured using electron backscatter diffraction (EBSD) in a field-emission scanning electron microscope (SEM, JSM-7001F, JEOL Inc.). The specimen surface was ion-polished for EBSD using a cross-section polisher (IB-09010CP, JEOL Inc.). Kikuchi patterns were collected at a working distance of 15 mm with an acceleration voltage of 15 kV using a TSL orientation imaging system. Due to the difficulty in indexing material with high dislocation density *via* conventional EBSD, the grain size of the UFG matrix was characterized using the transmitted Kikuchi diffraction (TKD) method described earlier.[27] A field-emission transmission electron microscope (TEM, JEM-2100F,



JEOL Inc.) was used to measure the grain size and identify small precipitates and dispersoids. A focused ion beam (FIB) system (JIB-4500, JEOL Inc.) was used to prepare thin TKD specimens and TEM thin foil specimens.

## 2.3. Mechanical Testing

Microhardness measurements were carried out using an FM-1e Vickers indenter with a maximum load of 200 gf and a dwell time of 10 s. The indents were made on a quarter surface of the disk with a spacing of 300  $\mu\text{m}$  because we assume that the microstructure is symmetrical with respect to the disk central axis. After the microhardness measurements, disks were cut using an electrical discharge machine into two miniature tensile specimens with gage lengths of 1 mm and thicknesses of 0.5 mm, as shown in Figure 1. Tensile tests were performed at room temperature with a constant strain rate ( $\sim 4.8 \times 10^{-4} \text{ s}^{-1}$ ) using a micro-tensile stage.[23] The yield strength, ultimate tensile stress (UTS), and elongation to fracture were calculated directly from the stress-strain curves. Fractured surfaces were investigated after tensile tests using SEM. However, due to limited materials, only one tensile specimen was tested for each sample.

## 3. RESULTS AND DISCUSSION

### 3.1. Microstructure Characterization

#### 3.1.1. Microstructure after cryomilling

Prior to HPT processing, the microstructure of the cryomilled trimodal AA 5083 composite exhibited CG regions with an average size of  $\sim 150 \mu\text{m}$  (area equivalent diameter) randomly dispersed in a UFG matrix, as shown in Figure 2(a). The spacing and the average aspect ratio of the CG regions were  $\sim 120$  and  $2.9 \mu\text{m}$ , respectively. The average grain sizes in the CG regions and the UFG matrix are listed in Table I. The dark contrast of the UFG matrix derives from the  $\text{B}_4\text{C}$  Y Zhang, S Sabbaghianrad, H Yang, T Topping, T Langdon, E Lavernia, J Schoenung, and S Nutt, “**Two-step SPD processing of a trimodal Al-based nano-composite**” Metall Trans Sept (2015) DOI: **10.1007/s11661-015-3151-6**





reinforcing particles ( $\sim 400$  nm) which generate a weak backscatter signal due to the low atomic number, as shown in Figure 2(b).  $\text{Al}_6(\text{Mn,Fe})$  dispersoids of similar size to  $\text{B}_4\text{C}$  particles were present in both CG regions and the UFG matrix, appearing as bright particles in Figure 2(b). These second-phase intermetallic particles (SPIPs) can alter the strength of the material *via* conventional Orowan strengthening. However, these second-phase particles may also reduce the fracture toughness because these brittle intermetallic particles may provide early crack nucleation sites under tension as shown in Figure 3. No pre-existing micro-cracks or voids were observed in the as-consolidated trimodal specimens, indicating that the Al powders can be effectively consolidated into a full density bulk sample using DMD forging.

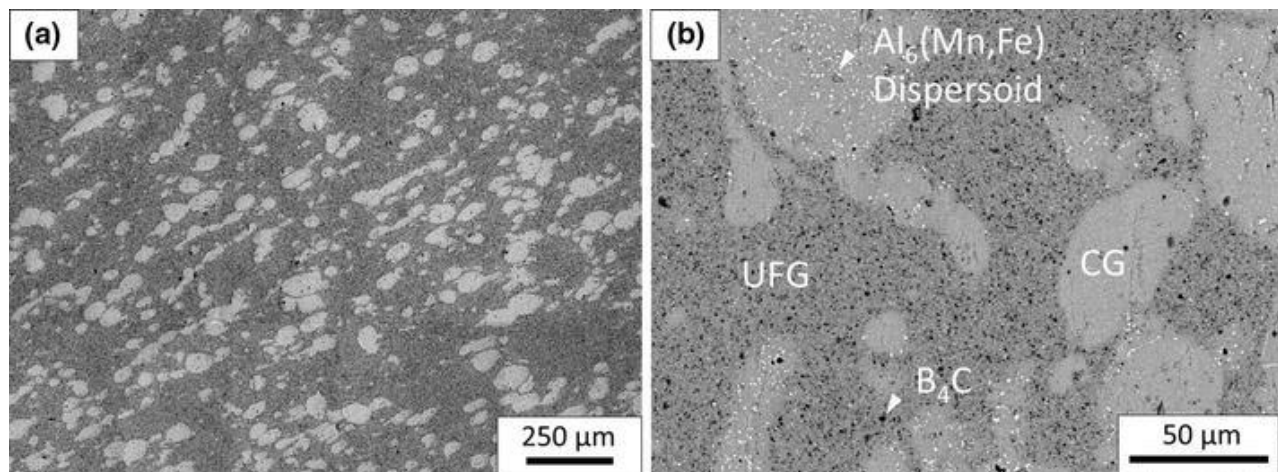


*Fig. 2 (a) Backscatter SEM micrograph of the trimodal structure, (b) Enlarged view of the microstructure showing UFG matrix with  $\text{B}_4\text{C}$  (dark particles) and CG regions with  $\text{Al}_6(\text{Mn,Fe})$  dispersoids (bright particles)*





*Table I Summary of the Microstructural Change as a Function of HPT Turns*

Sample ID	Avg. Grain Size	Avg. Grain Size	CG/ex-CG	CG/ex-CG Spacing (nm) <sup>a</sup>	B <sub>4</sub> C
	UFG (nm) <sup>a</sup>	CG/ex-CG (nm) <sup>a</sup>	Aspect Ratio <sup>a</sup>		Size (nm)
0T	441 ± 158	9191 ± 4502	2.9 ± 1.4	125.8 ± 45.0	409 ± 158
1/4T	283 ± 79	971 ± 487	5.6 ± 1.8	72.5 ± 37.6	384 ± 173
1T	177 ± 94	237 ± 134	7.6 ± 3.7	49.8 ± 31.9	418 ± 214
5T	204 ± 60	260 ± 52	24.2 ± 11.5	24.7 ± 8.2	439 ± 208

<sup>a</sup>All measurements were made near the edge of each HPT disk sample

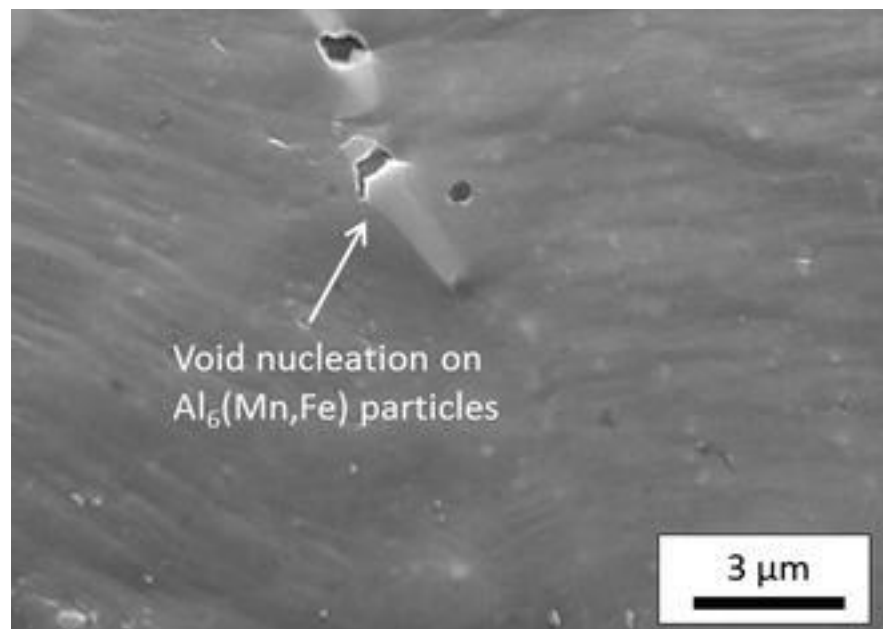


*Fig. 3 Secondary electron SEM image of a crack nucleation site on an intermetallic particle in the trimodal AA 5083 under tension*

### 3.1.2. Microstructure reshaping by HPT

To achieve more a desirable spacing and morphology of the CG regions, HPT was conducted on the cryomilled trimodal sample as a secondary SPD processing step. In the following context, the “cryomilling + HPT” processed trimodal samples and the “cryomilled-only” trimodal samples

Y Zhang, S Sabbaghianrad, H Yang, T Topping, T Langdon, E Lavernia, J Schoenung, and S Nutt, “**Two-step SPD processing of a trimodal Al-based nano-composite**” Metall Trans Sept (2015) DOI: **10.1007/s11661-015-3151-6**



will be designated as “ $nT$ ,” where  $n$  is the number of turns performed during HPT. Thus, a cryomilled sample processed with 1 turn of HPT is named “ $1T$ ” and the “cryomilled-only” sample is labeled “ $0T$ ” (without HPT processing).

The morphology of the CG regions was markedly altered by the shear strain during HPT. Figure 4 shows the microstructure of the HPT-processed samples. In these images, the bright and dark regions are the CG regions and the UFG matrix, respectively. The CG regions started deforming at the disk periphery, because the shear strain is a maximum at the edge during torsion.[30,31] As shown in Figures 4(a) through (c), the morphology of the CG regions evolved from oval shapes to a fine marbled pattern as the number of HPT turns increased. Figure 4(d) shows the microstructure of sample “ $5T$ .” The width and spacing of the CG strips are  $\sim 25\ \mu\text{m}$  which lies within the optimal size and spacing range ( $\sim 10$  to  $50\ \mu\text{m}$ ). The aspect ratio and spacing of the CG regions in each sample are summarized in Table I, where all the measurements were taken near the edge of the disk samples.

During HPT, both the UFG matrix and the CG regions experienced grain refinement together with increased dislocation density. As shown in Figure 5(a), sometimes a CG region exhibited a single-crystalline orientation accompanied by low-angle grain boundaries, an indication that some of the unmilled CG powders were single crystals prior to consolidation. The large shear strains applied during HPT introduced dislocations and reduced the grain size in these CG regions. The EBSD inverse pole figure images show a marked grain size reduction from an average size of  $9.2\ \mu\text{m}$  to  $971\ \text{nm}$  after  $1/4$  turn of HPT (see Figure 5(b)). After five turns of HPT, the average grain size of the CG regions dropped to  $\sim 260\ \text{nm}$  which is comparable to that of the UFG matrix. The black regions in Figure 5(b) are un-indexed due to poor quality Kikuchi patterns during EBSD



scans. This low pattern quality indicates a higher dislocation density introduced during HPT. The un-indexed regions comprised larger area fractions with increasing numbers of HPT turns. In the UFG matrix, the grain size was further reduced from ~450 to ~200 nm after HPT.

As shown in Figure 6, the grain size finally reached a constant value of ~250 nm for both the CG regions (Because CG regions no longer have coarse grains after HPT, we will rename them as “ex-CG regions” to avoid confusion) and the UFG matrix. It was not feasible to reduce the grain size further *via* more HPT turns because the strain-hardening rate was compensated by the dynamic recovery rate at such high strain levels. Grain size measurements (even using TKD) became difficult (un-indexed Kikuchi patterns) due to the high dislocation density and lattice distortion caused by shear strain during HPT. Therefore, the average grain size of “1T” and “5T” samples is only approximate due to the limited number of indexed grains. The size of B<sub>4</sub>C-reinforcing particles remained unchanged after HPT, as shown in Figure 6, because these hard brittle particles were effectively shielded by the softer UFG matrix during HPT. No cracks or voids were observed in the HPT-processed samples because of the high compression loading during HPT and strong Al/B<sub>4</sub>C interfaces.[32]

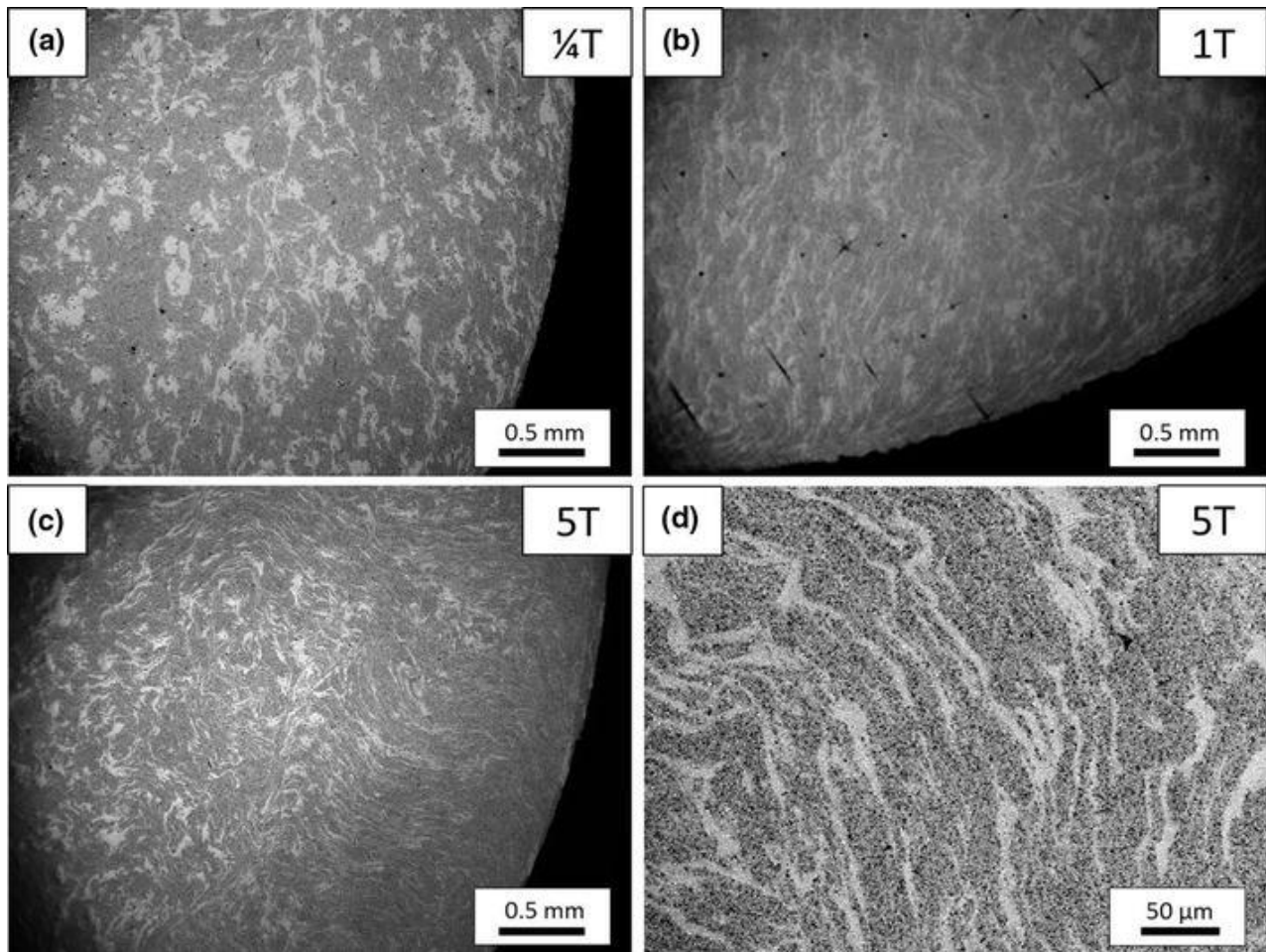


*Fig. 4 Light microscope images showing microstructure evolution after HPT of (a) 1/4T, (b) 1T, and (c) 5T. (d) Close-up view of the “5T” specimen*

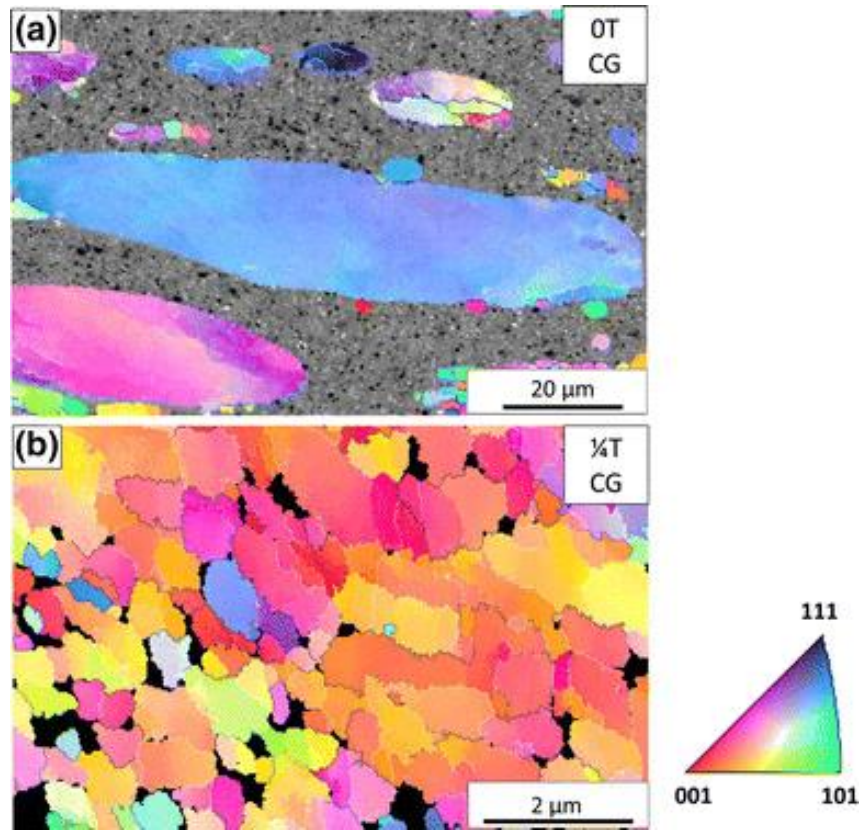


Fig. 5 (a) EBSD inverse pole figure map of the CG regions of sample “0T,” showing an average grain size of  $9.2\ \mu\text{m}$  in CG regions. (b) Grain size reduction (avg. grain size  $\sim 971\ \text{nm}$ ) in ex-CG regions after HPT (1/4T)

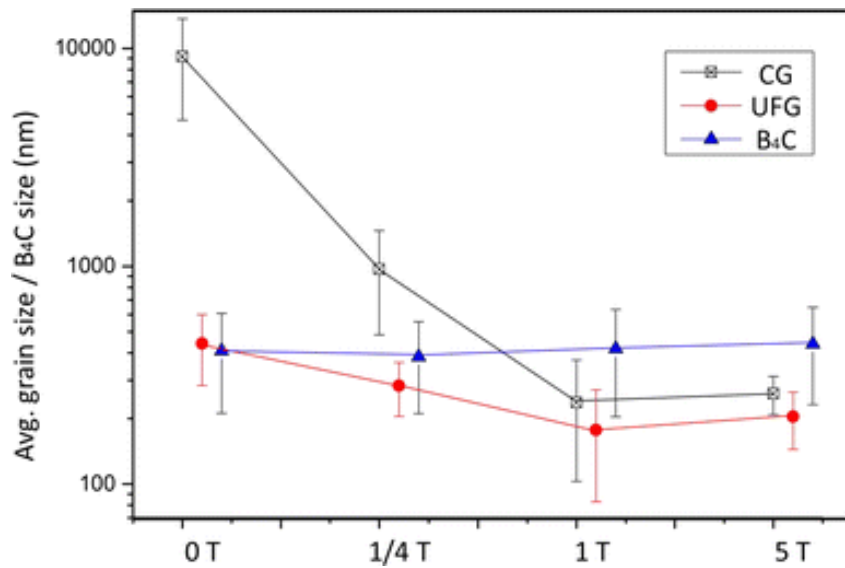


Fig. 6 Average grain size and B4C size plot as a function of HPT turns

Y Zhang, S Sabbaghianrad, H Yang, T Topping, T Langdon, E Lavernia, J Schoenung, and S Nutt, “Two-step SPD processing of a trimodal Al-based nano-composite” Metall Trans Sept (2015) DOI: 10.1007/s11661-015-3151-6





### 3.2. Microstructure Homogeneity

One potential drawback to HPT processing is the microstructural inhomogeneity that invariably arises from the radial strain gradient in the HPT disks in the early stages of HPT processing. Thus, a Vickers microhardness map was constructed to evaluate the hardness change and monitor the microstructural homogeneity among different areas of the disk. Only a quarter of the disk surface area was examined because it is reasonable to anticipate that the microstructure is symmetric with respect to the central axis of the disk. In Figure 7(a), the hardness map of sample “0T” shows an average hardness of  $\sim 120 H_v$  and the hardness variations stem from the heterogeneous trimodal structure. In Figure 7(b), sample “1/4T” exhibited a hardness increase ( $\sim 250 H_v$ ) starting from the edge, while the center of the disk remained unchanged because the 1/4 turn of HPT was insufficient to alter the microstructure near the disk center. As the number of turns increases, the hardness increases at both the disk edge and center, as shown in Figures 7(c) and (d), until there is saturation at  $\sim 300 H_v$ . This hardness saturation was consistent with the minimum grain size observed in Figure 6. Further torsional straining will not reduce the grain size and therefore will not increase the hardness. As shown in Figure 7(d), processing by HPT through five turns produced uniform hardness, grain size distribution, and ex-CG morphology throughout the disk except at the center of the disk. The miniature dog-bone tensile specimens were machined to avoid the center to ensure that the entire gage area had uniform microstructure.

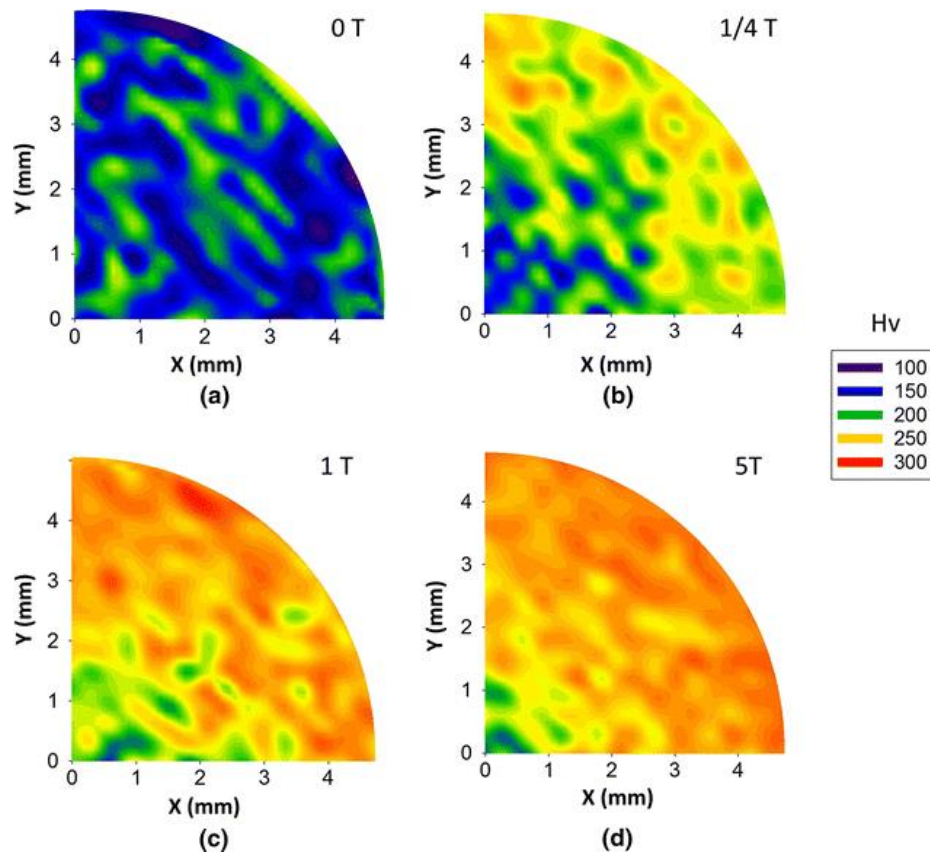


Fig. 7 Vickers microhardness map of a quarter surface of the HPT disks

### 3.3. Annealing

As discussed in Section III–A–2, the average grain size of the ex-CG regions approached that of the UFG matrix after several turns of HPT. As a result, the ductility of the ex-CG regions decreased, thereby limiting the toughening effect. To restore some of the ductility and toughening capacity, the HPT-processed trimodal AA 5083 was annealed to achieve recrystallization and grain growth in the ex-CG regions. Figure 8 shows the microstructures in the ex-CG regions after 1 hour annealing at 373 K, 473 K, 573 K, and 673 K (100 °C, 200 °C, 300 °C, and 400 °C). Recovery and recrystallization started at 373 K (100 °C), as shown in the inverse pole figure map (Figure 8(b)), which shows fewer un-indexed areas (dark region) compared to the non-annealed “5T” sample





(Figure 8(a)). Grain growth was observed in the ex-CG regions after annealing at 373 K (100 °C) and at higher temperatures (Figures 8(c) through (e)).

By contrast, the grain structure of the UFG matrix was preserved after annealing. Figure 9(a) shows an EBSD image quality map of sample “5T” after 1 hour annealing at 673 K (400 °C). The dark contrast in the UFG matrix indicates a low average intensity of the Hough peaks due to a high dislocation density and small grain size. Figure 9(b) is an STEM annular dark field image showing no significant grain growth in the UFG matrix of the annealed “5T” sample. This result indicates the thermal stability of the UFG matrix during annealing. In contrast, the CG regions (except for the grain boundaries) exhibit good quality metric [bright areas in Figure 9(a)], a result of reduced dislocation density and grain growth during annealing.

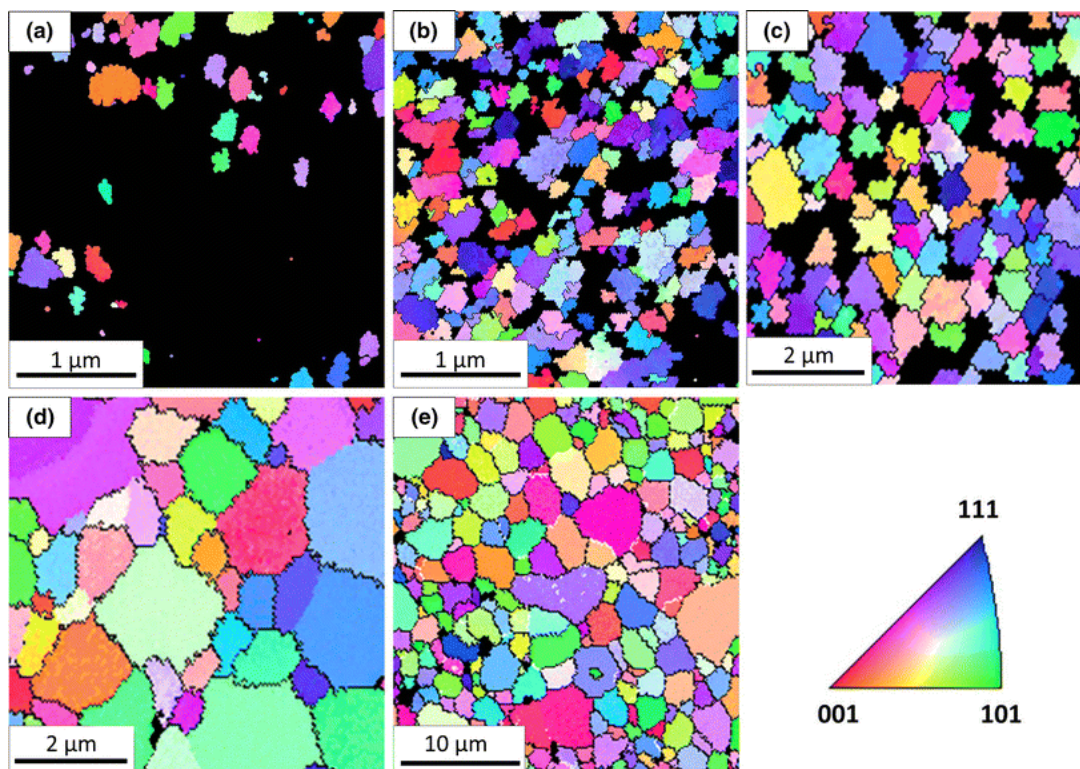


*Fig. 8 EBSD inverse pole figure maps of the ex-CG regions in (a) non-annealed “5T,” (b) “5T” annealed at 373 K (100 °C) for 1 h, (c) “5T” annealed at 473 K (200 °C) for 1 h, (d) “5T” annealed at 573 K (300 °C) for 1 h, and (e) “5T” annealed at 673 K (400 °C) for 1 h*

Y Zhang, S Sabbaghianrad, H Yang, T Topping, T Langdon, E Lavernia, J Schoenung, and S Nutt, “Two-step SPD processing of a trimodal Al-based nano-composite” *Metall Trans Sept* (2015) DOI: [10.1007/s11661-015-3151-6](https://doi.org/10.1007/s11661-015-3151-6)

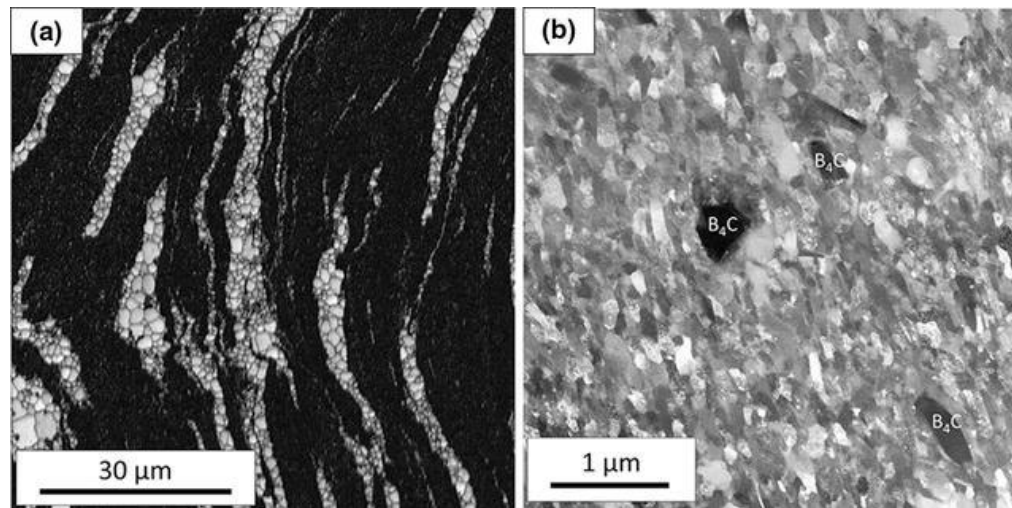


*Fig. 9 (a) EBSD image quality map of sample “5T” annealed at 673 K (400 °C) for 1 h, (b) STEM annular dark field image of the UFG matrix in the annealed “5T” sample*

The thermal stability of the UFG matrix is attributed to the presence of oxides and nitrides introduced during powder processing and cryomilling, respectively. These fine precipitates and solute segregated to grain boundaries and effectively pinned boundary movement and restricted dislocation glide.[33] The CG regions lacked thermal stability because the CG powders were not cryomilled and thus contained no oxide and nitride precipitates and solute to impede grain growth. Consequently, annealing restored the ductility of the CG regions without softening the thermally stable UFG matrix. Note that annealing in AA 5083 can potentially cause sensitization, a process in which magnesium segregates to grain boundaries to form  $\text{Al}_3\text{Mg}_2$  ( $\beta$  phase) intermetallic compounds. Sensitized AA 5083 is susceptible to both intergranular corrosion (IGC) and stress corrosion cracking (SCC), particularly in corrosive environments at high temperature ( $>50$  °C).[34–36]



### 3.4. Tension

Room temperature tensile tests were performed at a strain rate of  $\sim 4.8 \times 10^{-4} \text{ s}^{-1}$  using a micro-tensile stage. The tensile stress–strain curves for the “0T,” “1/4T” annealed at 673 K (400 °C), “1T” 673 K (400 °C), “5T” 673 K (400 °C), and a conventional work-hardened AA 5083 are plotted in Figure 10. The yield strength, ultimate tensile strength, and fracture elongation are listed in Table II. To eliminate the size effect of the tensile specimens, the properties listed in Table II were measured using identical specimen geometry and testing conditions. As shown in Figure 10(a), all trimodal AA 5083 samples exhibited high strength ( $>600 \text{ MPa}$ ), at least twice that of conventional AA 5083 ( $\sim 271 \text{ MPa}$ ). In particular, the annealed “5T” sample showed the highest yield strength ( $\sim 746 \text{ MPa}$ ), 24 pct greater than for sample “0T.” In addition, the “5T” sample annealed at 673 K (400 °C) showed the greatest elongation ( $\sim 1.9 \text{ pct}$ ) among all trimodal samples (Figure 10(b)). Note that this increase in both strength and elongation of the annealed “5T” sample is attributed to the change in the spacing and shape of the CG regions after HPT.

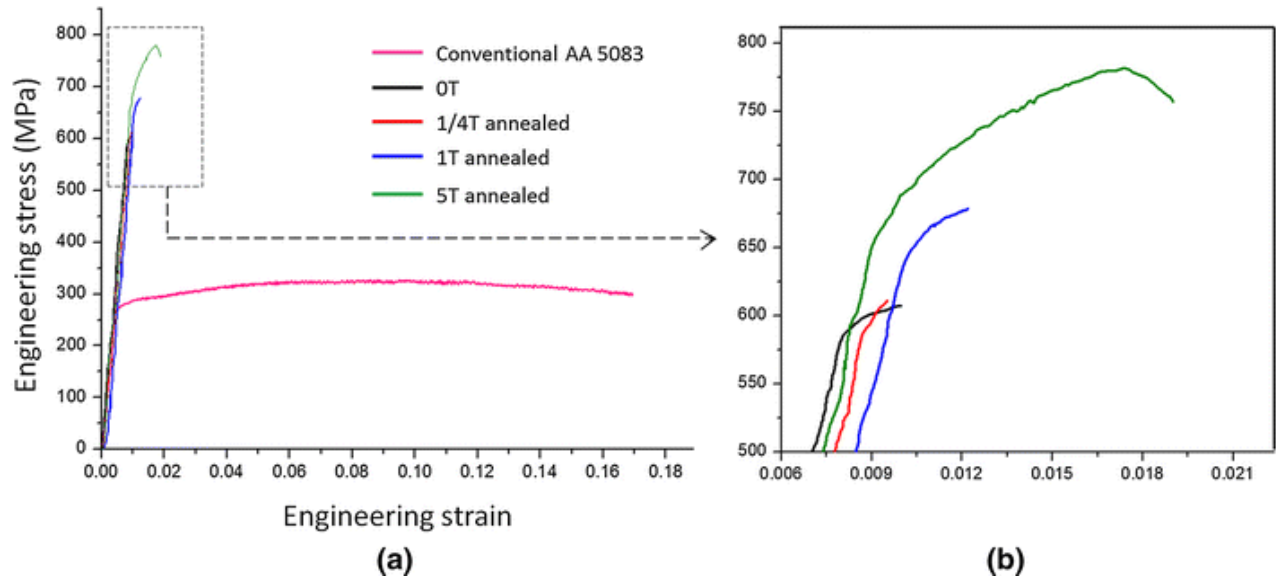


Fig. 10 (a) Tensile stress-strain curves of the conventional AA 5083, “0T,” “1/4T” [annealed at 673 K (400 °C)], “1T” [annealed at 673 K (400 °C)], and “5T” [annealed at 673 K (400 °C)], (b) partial enlargement of the stress–strain curves near fracture

Table II List of the Tensile Properties Measured from the Stress–Strain Curves

Sample ID	Yield Strength (MPa)	Ultimate Tensile Stress (MPa)	Fracture Elongation (pct)
Conventional AA 5083	271	324	16.9
0T	603	607	1.0
1/4T annealed at 673 K (400 °C)	—	611	1.0
1T annealed at 673 K (400 °C)	677	678	1.2
5T annealed at 673 K (400 °C)	746	781	1.9

### 3.5. Fracture Mechanism

Fracture surfaces were examined after tensile tests to determine failure mechanisms. Two distinctive failure modes were evident in the ductile CG regions and the brittle UFG matrix as shown in Figure 11, where CG regions are artificially tinted to enhance visibility. Figures 11(a) and (b) is the fracture surfaces of samples “0T” and “5T” (annealed at 673 K (400 °C)),





respectively. The CG regions of sample “0T” were elongated perpendicular to the forging direction. In contrast, the CG regions of sample “5T” (annealed at 673 K (400 °C)) had smaller spacings and no preferred direction of elongation. Figure 11(c) shows brittle intergranular fracture observed in the UFG matrix. The CG region in Figure 11(c) shows a dimple and cup fracture surface, an indication of ductile failure.

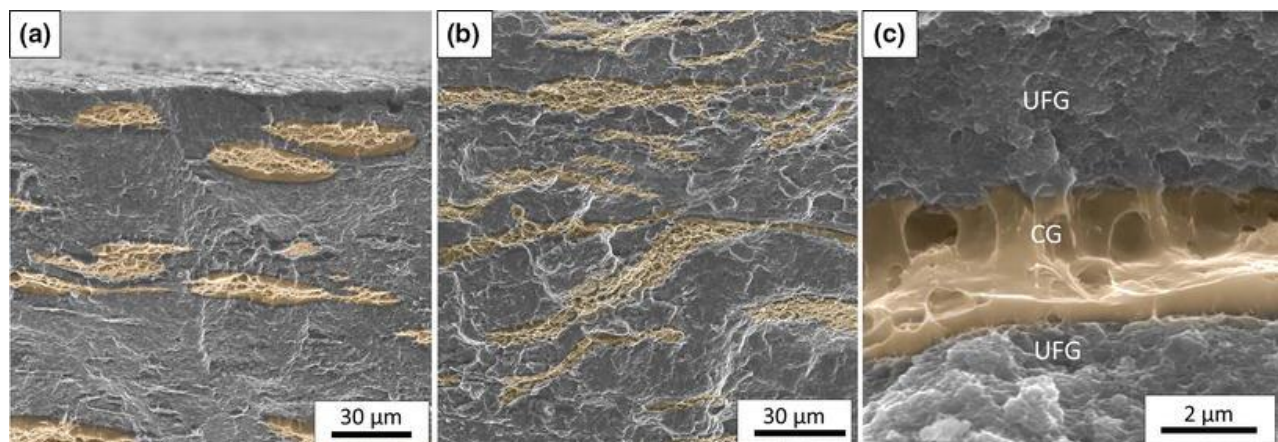


*Fig. 11 Fracture surfaces of (a) “0T” and (b) “5T” (annealed at 673 K (400 °C)) with artificially tinted CG regions. (c) SEM Micrograph showing intergranular fracture in the UFG matrix and dimple-like ductile fracture in the CG region of sample “5T” [annealed at 673 K (400 °C)]*

Figure 12 schematically shows the toughening process of the CG regions in sample “5T” (annealed at 673 K (400 °C)). First, the majority of micro-cracks initiated at the brittle intermetallic dispersoid sites under tensile loading. Because the spacing of the CG regions was intentionally reduced to the plastic zone size of the UFG matrix,[27] the crack growth was effectively retarded due to a toughening mechanism in adjacent CG regions, as shown in Figure 13, where a surface micro-crack was arrested at a CG region. This delay in crack propagation led to the extended uniform elongation and therefore higher strength of sample “5T” [annealed at 673 K (400 °C)], as shown in Figure 10(b). As the load increased, micro-cracks grew and interconnected, quickly leading to catastrophic fracture. The limited yielding and strain softening



recorded in the stress-strain curve (Figure 10) were attributed to the local necking of the CG regions, as shown in Figure 12(b). Sample “5T” (annealed at 673 K (400 °C)) exhibits a slightly higher ductility (Figure 10). More CG regions were involved in toughening and thus contributed to a higher elongation compared to sample “0T” in which a crack readily avoided the CG regions and found “easy” propagation pathways in the UFG matrix.

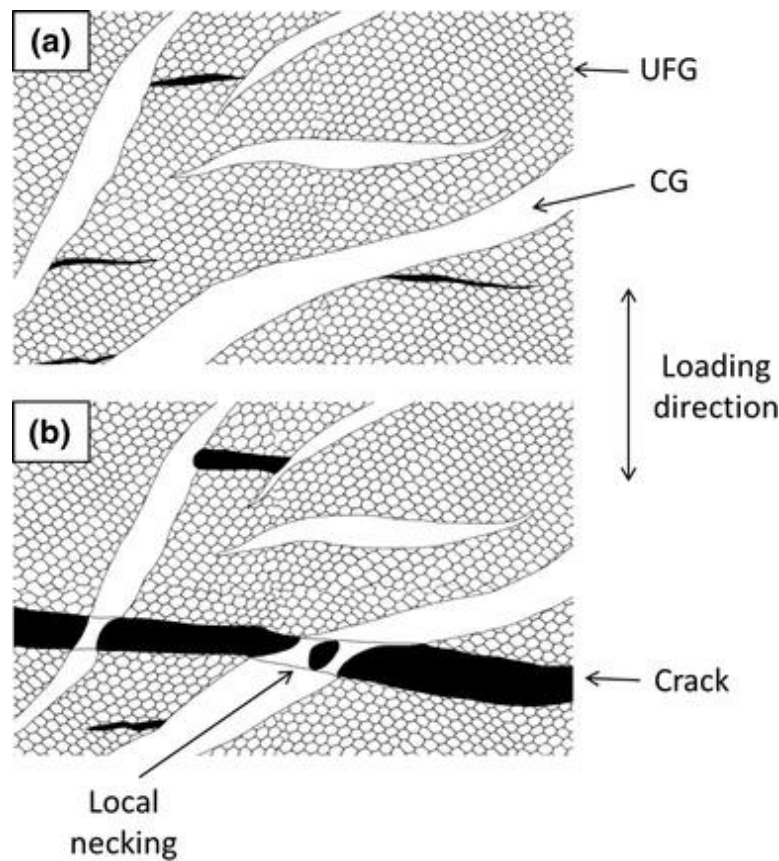


*Fig. 12 Schematic illustration of the failure mechanisms in sample “5T” [annealed at 673 K (400 °C)]*

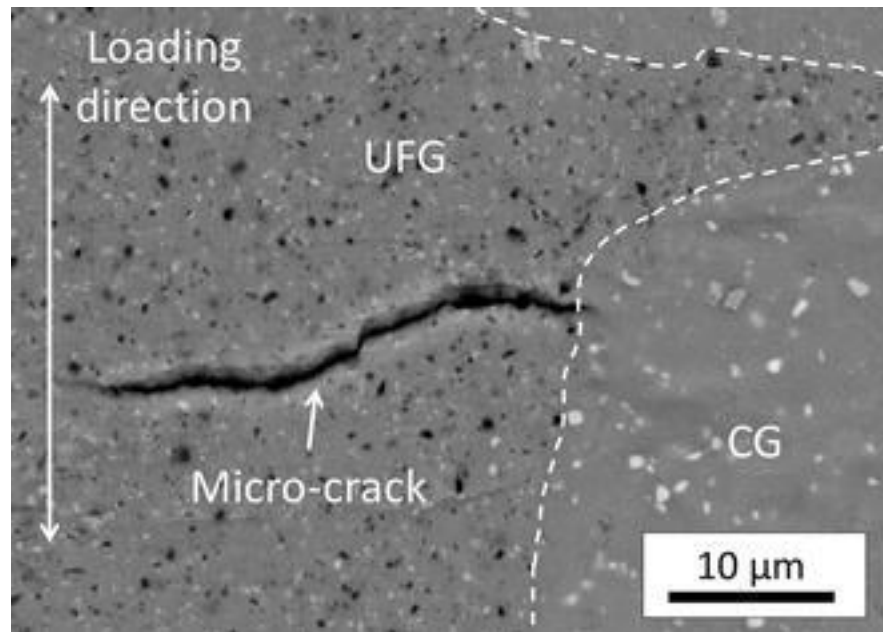


*Fig. 13 Backscatter image of a surface micro-crack stopped at a CG region*

#### 4. CONCLUSIONS

Most toughening strategies for ultrafine-grained materials enhance ductility while sacrificing some amount of strength. In this work, we demonstrated that the strength and ductility of trimodal AA 5083 composites (although still limited compared to conventional AA 5083) can be improved simultaneously by judicious control of the spacing and morphology of the CG regions. Increasing HPT turns (*e.g.*, 20 turns) may lead to even higher strength and ductility by activating new deformation mechanisms (*e.g.*, grain boundary sliding) in the UFG matrix.[37–39] The thermally stable nature of the UFG matrix leads to selective grain growth in the ex-CG regions and introduces a potential for high temperature applications for this material. However, this trimodal AA 5083 composite may not be suitable for use in corrosive environments due to possible susceptibility to stress corrosion cracking ( $\text{Al}_3\text{Mg}_2$  precipitates introduced during thermomechanical processing and subsequent annealing). In addition, the two-step SPD synthesis involves multiple steps and processing variables that will inevitably entail high-cost and low-yield

Y Zhang, S Sabbaghianrad, H Yang, T Topping, T Langdon, E Lavernia, J Schoenung, and S Nutt, “**Two-step SPD processing of a trimodal Al-based nano-composite**” *Metall Trans* Sept (2015) DOI: **10.1007/s11661-015-3151-6**





production. A major practical limitation of HPT arises from the thin-plate geometry, a factor that will limit engineering applications. Alternative fabrication techniques will be required to reduce the production cost and remove the geometry limitation. Nevertheless, this work validates the toughening strategy in which strong and hard phases, when combined with ductile regions of optimal size and spacing, effectively increase strength while retaining acceptable toughness. The trimodal microstructure described here can only be achieved through powder processing routes that allow tailoring of multi-modal grain size distributions. These routes expand the design space for materials with mixed microstructures and balanced properties not achievable by conventional routes. It is anticipated that refinements of this approach will lead to bulk materials having the toughness levels required for load-bearing structures ( $\sim 20 \text{ MPa} \cdot \text{m}^{1/2}$ – $20 \text{ MPa} \cdot \text{m}^{1/2}$ ), while simultaneously boosting the strength to  $\sim 700 \text{ MPa}$ , thereby overcoming the strength-ductility paradox of UFG materials.

**Acknowledgements:** The authors gratefully acknowledge M. Mecklenburg for his help in TEM. The images and data used in this article were generated at the Center for Electron Microscopy and Microanalysis (CEMMA), University of Southern California. The authors wish to acknowledge financial support provided by the Office of Naval Research under the guidance of Rod Peterson and Bill Golumbskie (ONR Contract N00014-12-C-0241), the National Science Foundation of the United States under Grant No. DMR-1160966, and the European Research Council under ERC Grant Agreement No. 267464-SPDMETALS.

## **References:**

1. R. Z. Valiev, R. K. Islamgaliev, and I. V. Alexandrov, *Prog. Mater. Sci.*, vol. 45, no. 2, pp. 103–189, Mar. 2000.
2. R. Kapoor and J. K. Chakravartty, *Acta Mater.*, vol. 55, pp. 5408–5418, 2007.
3. T. G. Langdon, *Acta Mater.*, vol. 61, no. 19, pp. 7035–7059, 2013.

Y Zhang, S Sabbaghianrad, H Yang, T Topping, T Langdon, E Lavernia, J Schoenung, and S Nutt, “**Two-step SPD processing of a trimodal Al-based nano-composite**” *Metall Trans Sept* (2015) DOI: **10.1007/s11661-015-3151-6**



4. T. G. Langdon, *Mech. Mater.*, vol. 67, pp. 2–8, 2013.
5. Y. Huang and T. G. Langdon, *Mater. Today*, vol. 16, no. 3, pp. 85–93, 2013.
6. L. S. Toth and C. Gu, *Mater. Charact.*, vol. 92, pp. 1–14, 2014.
7. R. Z. Valiev, Y. Estrin, Z. Horita, T. G. Langdon, M. J. Zehetbauer, Y. T. Zhu, *JOM*, vol. 58, no. 4, pp. 33–39, 2006.
8. E.O. Hall, *Proc. Phys. Soc.*, vol. B64, pp. 747–753, 1951.
9. N.J. Petch, *J. Iron Steel Inst.*, vol. 174, pp. 25–28, 1953.
10. Y.T. Zhu and T.G. Langdon, *JOM*, vol. 56 (10), pp. 58–63, 2004.
11. Y.T. Zhu, T.C. Lowe, T.G. Langdon, *Scripta Mater.*, vol. 51, pp. 825–830, 2004.
12. R.Z. Valiev, A.P. Zhilyaev, and T.G. Langdon: *Bulk Nanostructured Materials: Fundamentals and Applications*. Wiley, Hoboken, 2014.
13. A. P. Newbery, S. R. Nutt, and E. J. Lavernia, *JOM*, vol. 58 (4), pp. 56–61, 2006.
14. A. P. Newbery, B. Ahn, T. D. Topping, P. S. Pao, S. R. Nutt, and E. J. Lavernia, *J. Mater. Process. Technol.*, vol. 203 (1–3), pp. 37–45, Jul. 2008.
15. D. Witkin, B.Q. Han, and E.J. Lavernia, *Metall. Mater. Trans. A*, vol. 37A, pp. 185–194, 2006.
16. D. B. Witkin and E. J. Lavernia, *Prog. Mater. Sci.*, vol. 51, no. 1, pp. 1–60, Jan. 2006.
17. R. W. Hayes, P. B. Berbon, and R. S. Mishra, *Metall. Mater. Trans. A*, vol. 35A (12), pp. 3855–3861, 2004.
18. O. Susegg, *Micron and Microscopica Acta*, vol. 23(1/2), pp. 223–224, 1992.
19. Y. Li, W. Liu, V. Ortolan, W. F. Li, Z. Zhang, R. Vogt, N. D. Browning, E. J. Lavernia, and J. M. Schoenung, *Acta Mater.*, vol. 58 (5), pp. 1732–1740, 2010.
20. G. J. Fan, H. Choo, P. K. Liaw, and E. J. Lavernia, *Acta Mater.*, vol. 54, no. 7, pp. 1759–1766, Apr. 2006.
21. Z. Lee, V. Radmilovic, B. Ahn, E. J. Lavernia, and S. R. Nutt, *Metall. Mater. Trans. A*, vol. 41, no. 4, pp. 795–801, Oct. 2009.
22. Z. Lee, D. B. Witkin, V. Radmilovic, E. J. Lavernia, and S. R. Nutt, *Mater. Sci. Eng. A*, vol. 410–411, pp. 462–467, Nov. 2005.
23. Y. Zhang, T. D. Topping, E. J. Lavernia, and S. R. Nutt, *Metall. Mater. Trans. A*, vol. 45, no. 1, pp. 47–54, May 2013.
24. L. Jiang, K. Ma, H. Yang, M. Li, E. J. Lavernia, and J. M. Schoenung, *JOM*, vol. 66, no. 6, pp. 898–908, Apr. 2014.
25. Z. Zhang, T. D. Topping, Y. Li, R. Vogt, Y. Zhou, C. Haines, J. Paras, D. Kapoor, J. M. Schoenung, and E. J. Lavernia, *Scr. Mater.*, vol. 65, no. 8, pp. 652–655, Oct. 2011.
26. J. Ye, B. Q. Han, Z. Lee, B. Ahn, S. R. Nutt, and J. M. Schoenung, *Scr. Mater.*, vol. 53, no. 5, pp. 481–486, Sep. 2005.
27. Y. Zhang, T. D. Topping, H. Yang, E. J. Lavernia, J. M. Schoenung, and S. R. Nutt, *Metall. Mater. Trans. A*, vol. 46, pp. 1196–1204, 2015.
28. D. C. Hofmann, J.Y. Suh, A. Wiest, G. Duan, M.L. Lind, M. D. Demetriou, and W. L. Johnson, *Nature*, vol. 451, no. 7182, pp. 1085–9, Feb. 2008.
29. A.P. Zhilyaev, T.G. Langdon, *Prog. Mater. Sci.*, vol. 53, pp. 893–979, 2008.
30. R. Z. Valiev, Y. V. Ivanisenko, E. F. Rauch, B. Baudelet, *Acta Mater.*, vol. 44, pp. 4705–4712, 1996.



31. F. Wetscher, A. Vorhauer, R. Stock, R. Pippan, *Mater. Sci. Eng. A*, vol. 387-389, pp. 809-816, 2004.
32. Y. Li, Z. Zhang, R. Vogt, J. M. Schoenung, and E. J. Lavernia, *Acta Mater.*, vol. 59, no. 19, pp. 7206–7218, Nov. 2011.
33. L. Hashemi-Sadraei, S. E. Mousavi, R. Vogt, Y. Li, Z. Zhang, E. J. Lavernia, and J. M. Schoenung, *Metall. Mater. Trans. A*, vol. 43 (2), pp. 747–756, 2012.
34. Y. Zhu, D. A. Cullen, S. Kar, M. L. Free, and L. F. Allard, *Metall. Mater. Trans. A*, vol. 43, no. 13, pp. 4933–4939, Aug. 2012.
35. S. Jain, M. L. C. Lim, J. L. Hudson, and J. R. Scully, *Corros. Sci.*, vol. 59, no. 2012, pp. 136–147, Jun. 2012.
36. I. N. A. Oguocha, O. J. Adigun, and S. Yannacopoulos, *J. Mater. Sci.*, vol. 43, no. 12, pp. 4208–4214, Apr. 2008.
37. R. Z. Valiev and I. V. Alexandrov, Y. T. Zhu, T. C. Lowe, *J. Mater. Res.*, vol. 17, no. 1, pp. 5–8, 2002.
38. T. Mungole, P. Kumar, M. Kawasaki, and T. G. Langdon, *J. Mater. Res.*, vol. 29, no. 21, pp. 2534–2546, Oct. 2014.
39. T. Mungole, P. Kumar, M. Kawasaki, and T.G. Langdon, *J. Mater. Sci.*, vol. 50, pp. 3549-3561, 2015.